



Acta Materialia 57 (2009) 722-731



www.elsevier.com/locate/actamat

# TEM and XPS analysis of $Ca_xCe_{1-x}O_{2-y}$ (x = 0.05-0.5) as electrolyte materials for solid oxide fuel cells

M. Yan<sup>a,\*</sup>, T. Mori<sup>a</sup>, J. Zou<sup>b,c</sup>, F. Ye<sup>a</sup>, D.R. Ou<sup>a</sup>, J. Drennan<sup>c</sup>

<sup>a</sup> Fuel Cell Materials Center, National Institute for Materials Science, 1-1 Namiki, Tsukuba, Ibaraki 305-0044, Japan
 <sup>b</sup> School of Engineering, The University of Queensland, Brisbane, Qld 4072, Australia
 <sup>c</sup> Centre for Microscopy and Microanalysis, The University of Queensland, Brisbane, Qld 4072, Australia

Received 14 May 2008; received in revised form 9 October 2008; accepted 10 October 2008 Available online 17 November 2008

#### Abstract

The microstructure and conductivity property of Ca-doped CeO<sub>2</sub> were studied in a wide range of dopant concentrations (from 5 to 50 at.%). Through detailed transmission electron microscopy and X-ray photoelectron spectroscopy investigations, we determined the secondary phase besides the doped ceria, clarified the solubility limit for the dopant and specified the reduction behavior of CeO<sub>2</sub> induced by the Ca doping and the associated reduction product. The influences of the microstructures on the ionic conductivity of Ca-doped CeO<sub>2</sub> are discussed, from which the optimal doping level of Ca is suggested.

© 2008 Acta Materialia Inc. Published by Elsevier Ltd. All rights reserved.

Keywords: Solid electrolytes; Microstructure; Transmission electron microscopy (TEM); X-ray photoelectron spectroscopy (XPS); CeO<sub>2</sub>

#### 1. Introduction

Doped ceria materials have been the focus of global attention in recent decades as a result of their wide potential applications [1,2]. In particular, ceria doped with rare earth elements (e.g. Gd) and alkaline earth elements (e.g. Ca) have gained significant attention as promising candidates in the fields of catalysts [3], oxygen sensors [4] and solid oxide fuel cells (SOFCs) [5–7].

With respect to SOFCs, the electrolytes based on Ca-doped CeO<sub>2</sub> have two major advantages over those doped using rare earth elements [7–9]: (i) they are less of an environmental burden, since much less effort is required to mine and extract Ca from minerals when compared with the rare earth elements and (ii) they have a significantly lowered production cost, since Ca is naturally abundant. These advantages suggest that Ca-doped CeO<sub>2</sub> electrolytes could be a more sustainable choice than the rare-earth-doped CeO<sub>2</sub> in the long term.

E-mail address: YAN.Ming@nims.go.jp (M. Yan).

It should be noted that previous studies on Ca-doped CeO<sub>2</sub> focused mainly on the ionic conductivity [8–12], with little attention being paid to microstructural variations. This contrasts with studies on rare-earth-doped CeO<sub>2</sub> materials, where a considerable number of detailed microstructure studies have been undertaken. For examples, Gd-, Sm-, Y- and Tb-doped CeO<sub>2</sub> have all been studied extensively. From these studies, it is clear that microstructural control of doped ceria materials is a key factor in determining and understanding their ionic conducting performance [13–16]. As a consequence, it is important to develop a similar understanding for Ca-doped CeO<sub>2</sub>, so that microstructural engineering can be used to optimize their conduction properties.

In this study, detailed microstructural characterization of Ca-doped CeO<sub>2</sub> over a wide dopant concentration range  $[Ca_xCe_{1-x}O_{2-y} \ (x=0.05-0.5)]$  was performed, in which transmission electron microscopy (TEM) and X-ray photoemission spectroscopy (XPS) were comprehensively employed to understand the microstructural evolution of Ca-doped CeO<sub>2</sub> with increasing dopant concentration. Specifically, XPS is a powerful tool with which to investigate

<sup>\*</sup> Corresponding author.

the chemical state and microstructure of materials, and has been widely used to study the reduction behavior of undoped CeO<sub>2</sub> (e.g. [17]) and rare-earth-doped CeO<sub>2</sub> (e.g. [18]). Through such an investigation, the microstructural variation in Ca-doped CeO<sub>2</sub> as a function of the dopant concentration has been determined.

# 2. Experimental

# 2.1. Materials synthesis

As precursors, the nanosized powders of  $Ca_xCe_{1-x}O_{2-y}$ (x = 0.05, 0.1, 0.2, 0.3, 0.4, 0.5) were prepared by a co-precipitation method [19,20]. High-purity (>99.99%) cerium nitrate hexhydrate [Ce(NO<sub>3</sub>)<sub>3</sub>·6H<sub>2</sub>O], calcium nitrate tetrahydrate [Ca(NO<sub>3</sub>)<sub>2</sub>·4H<sub>2</sub>O] and ammonium carbonate [(NH<sub>4</sub>)<sub>2</sub>CO<sub>3</sub>] were used in the experiment. The ratio between the cations and the carbonate was 4-6, and the precipitation was carried out at a temperature of 40–50 °C. The obtained precursor powders were firstly calcined at 700 °C for 2 h and then compacted into pellets  $(\Phi \sim 10 \times 3 \text{ mm})$  under a rubber press of  $\sim 15 \text{ MPa}$ . The compacted pellets were subsequently sintered at 1100 °C for 4 h before being cooled to room temperature. Hereafter, abbreviated terms, e.g. 5Ca for the sample of 5 at.% Ca, will be used for convenience. The density of the sintered pellets was measured by the Archimedes method, indicating a high density ( $\sim$ 95% of the theoretical density) for 5Ca-30Ca and a comparatively lower density for 40Ca and 50Ca. Bulk conductivities of the sintered pellets were measured via the three probes DC technique in air between 400 and 700 °C.

## 2.2. Microstructural analyses

XPS was conducted in a PHI 5700 ESCA system with a chamber pressure of  $5-8 \times 10^{-9}$  Torr. Undoped CeO<sub>2</sub> was used as a reference in the XPS analysis, which was prepared in a way similar to the Ca-doped CeO<sub>2</sub>. A monochromatic Al  $K_{\alpha}$  X-ray (1486.6 eV) was used as the incident radiation. The survey spectrum was recorded at a pass energy of 187.85 eV, and the high resolution analysis was conducted at a pass energy of 29.35 eV. The instrumental error in terms of the binding energy was within  $\pm 0.1$  eV. Both the original surface and the Ar-ion sputtered surface were analyzed by XPS, and the latter was carried out by etching off a layer of  $\sim$ 5 nm from the original surface. The software, PC-ACCESS, was used to analyze the recorded XPS spectra. In particular, the Gaussian-Lorentzian method was employed to fit experimental curves and the background was subtracted by an integration method.

TEM was performed on a JEOL NM-200 and operated at 200 kV. Scanning electron microscopy (SEM; Hitachi S-5000, 10 kV and Hitachi S-5800, 20 kV) and X-ray diffractometry (XRD; Rigaku RINT 2000HF Ultima, 40 kV/40 mA, Cu  $K_{\alpha}$  radiation) were also used for the microstructural analyses.

## 3. Results

#### 3.1. Microstructure characterization by XRD and SEM

Fig. 1 shows the XRD patterns for the sintered pellets and indicates that the fluorite structured doped ceria is the dominant phase. As can also be seen from the figure, additional diffraction peaks appear when the dopant concentration reaches 30 at.%; the higher the dopant concentration, the stronger the extra diffraction peaks. The fact that the positions of these extra diffraction peaks remain the same with different dopant concentrations (e.g. the major diffraction peaks are all shown at  $2\theta$  angles of  $\sim 37$ ,  $\sim 54$  and  $\sim 32^\circ$ ; see the inset for details) suggests that the secondary phase developed in these heavily Ca-doped CeO<sub>2</sub> should be identical.

Systematic SEM investigations were subsequently performed and Fig. 2 presents the SEM backscattered electron (SEM-BSE) images for 10Ca-50Ca. As can be seen, the SEM-BSE image is basically uniform at the dopant concentration of 10 at.% (Fig. 2(a)), suggesting no compositional segregation. However, for the dopant concentration of 20 at.%, the secondary phase can be clearly observed as a dark contrast when compared with the doped ceria (Fig. 2(b)). The corresponding SEM X-ray mapping indicates that the composition of the secondary phase contains more Ca but less Ce and O when compared with the doped ceria (Fig. 2(c) presents the corresponding Ca map). By comparing the SEM-BSE images taken from 20Ca-50Ca, it is evident that the amount of the secondary phase increases with increasing dopant concentration. Moreover, no remarkable compositional variations can be found in these phases, suggesting that they should be identical. This is consistent with the XRD results, although the XRD

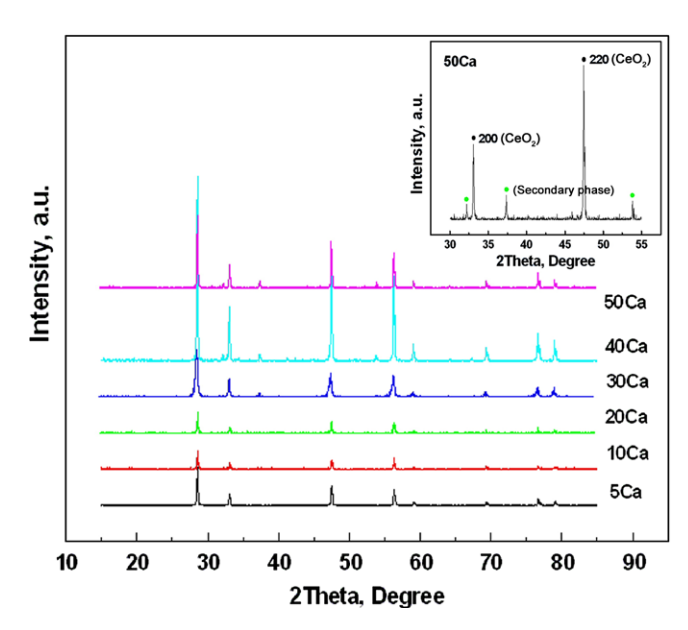


Fig. 1. XRD patterns of the sintered pellets. The inset shows additional diffraction peaks besides the main diffraction peaks from the doped ceria.

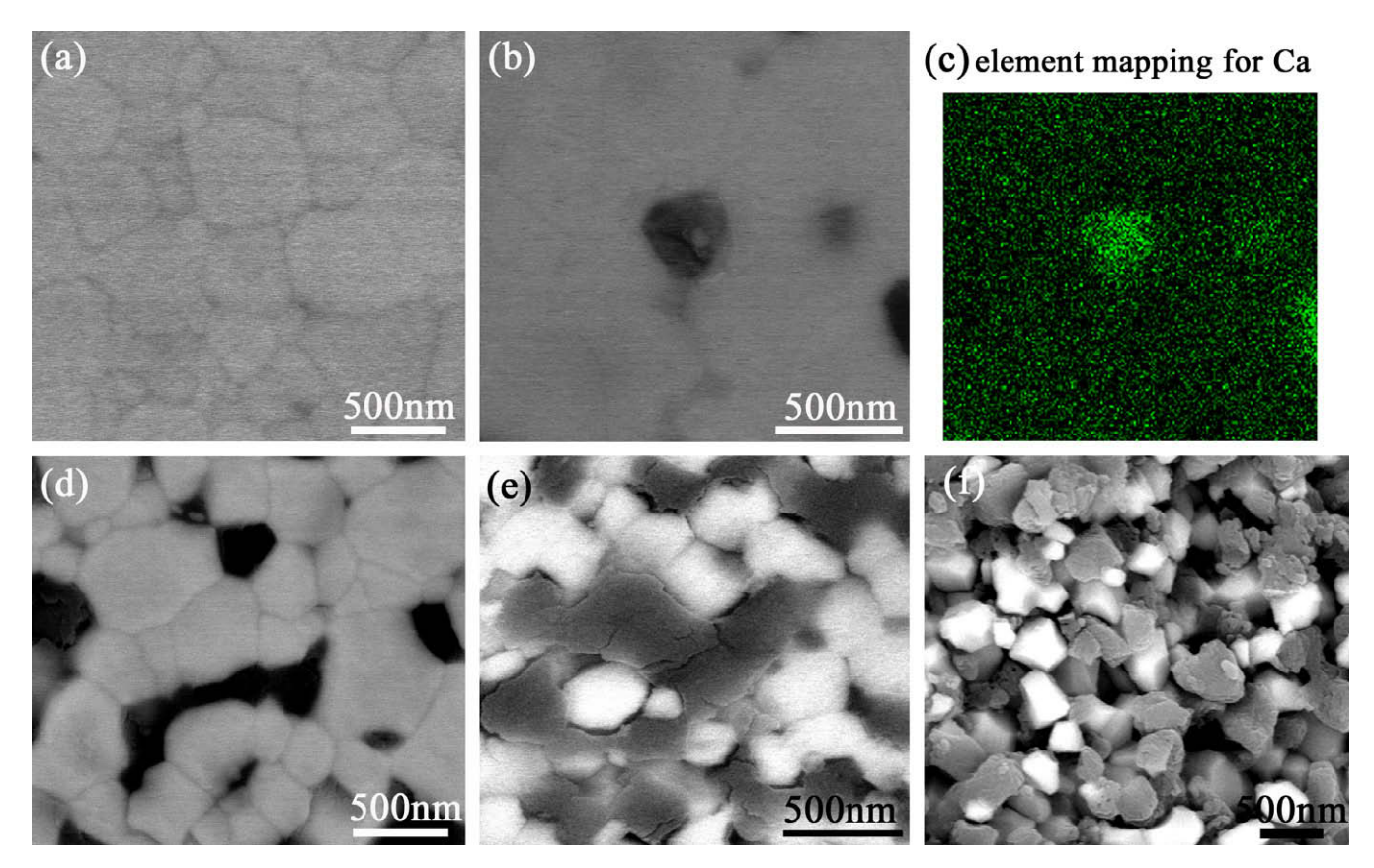


Fig. 2. SEM-BSE images showing the morphologies of the sintered pellets: (a) 10Ca, (b) 20Ca, (c) Ca elemental map in 20Ca, (d) 30Ca, (e) 40Ca and (f) 50Ca.

pattern for 20Ca does not clearly show the existence of the secondary phase, indicating that the amount of the secondary phase is low and beyond the XRD's detectability.

# 3.2. XPS analysis

To further understand the microstructure and the chemical state of Ca-doped CeO2, XPS was employed. Fig. 3 shows typical XPS spectra with the binding energy (BE) in the range of 0-1200 eV for both the original and the sputtered 5Ca. As can be seen, as well as the expected elements of Ce, Ca and O, additional peaks from C are detectable in both cases, which probably resulted from environmental contamination. Nevertheless, the spectra can be used as references to calibrate the peak position of other elements by assuming that the C 1s peak is located at the BE of 285 eV [21]. Additionally, it was found that a higher level of carbon contamination was always encountered in the original surface and the Ce 3d signals in the original surface were always less clear when compared with the sputtered surface. Therefore, only the experimental results from the sputtered samples are discussed.

Fig. 4(a) shows the Ce 3d spectra for all samples. It can be seen that the samples with high dopant concentrations show a comparatively decreased area fraction of the u''' peak that belongs to the Ce<sup>4+</sup> state exclusively [22]. Based on this, a reduction from Ce<sup>4+</sup> towards Ce<sup>3+</sup> is expected. It

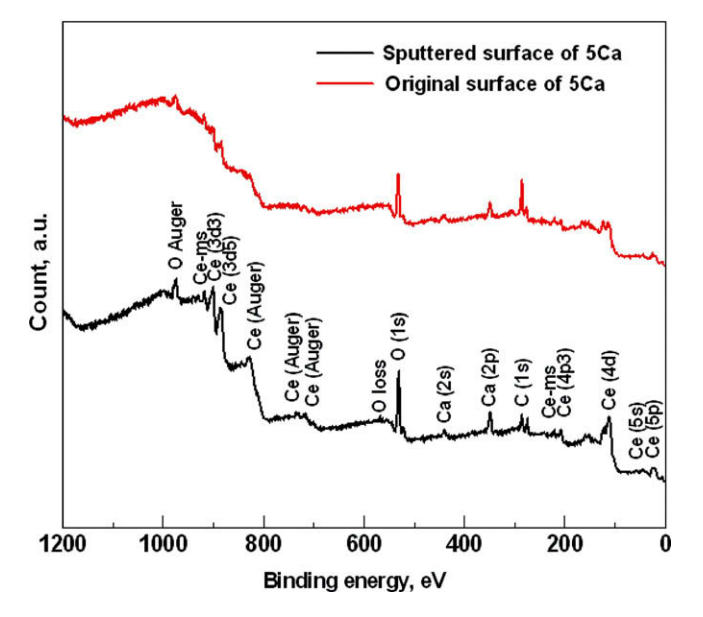


Fig. 3. XPS survey spectra of the original and the Ar-ion sputtered 5Ca samples.

should be mentioned that it is difficult to quantitatively determine the  $Ce^{4+}$  fraction due to the complexity of the Ce 3d spectrum (resulted from pairs of three spin-orbit splits with different final-state configurations of  $4f^n$  (n = 0, 1, 2)) [22] and there is no single way to solve this problem [23,24]. As a consequence, the following pathway

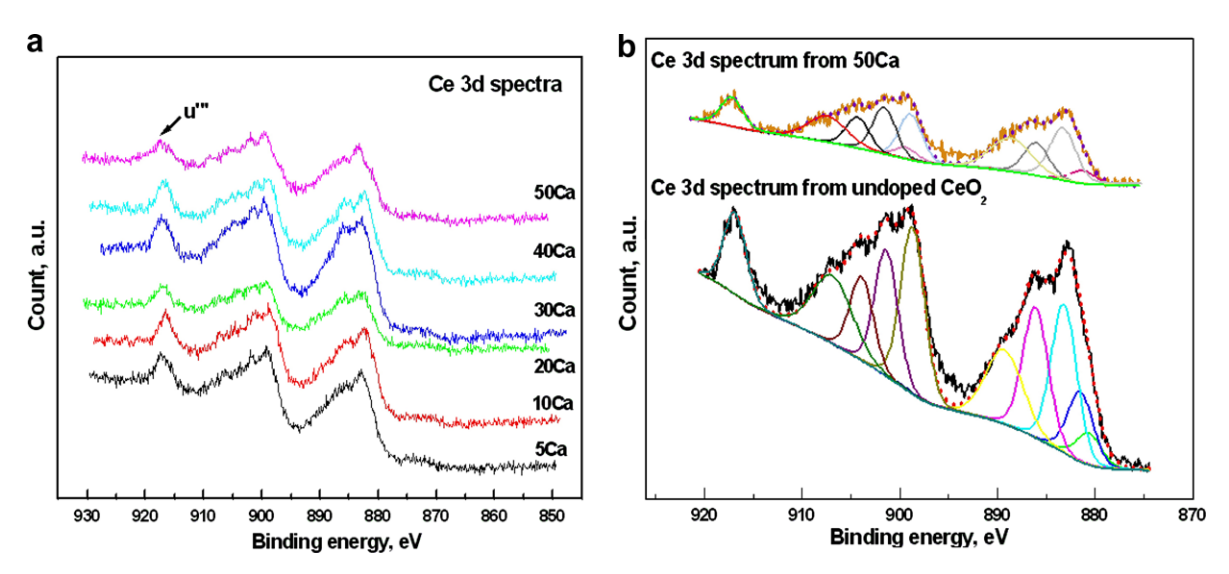


Fig. 4. XPS results for the sintered pellets: (a) Ce 3d spectra, in which the u''' peak is marked by an arrow and (b) deconvolution results for the undoped CeO<sub>2</sub> and 50Ca. Dotted lines represent the fitting curves.

was used in this study to estimate the reduction of Ce ions. First, we used an undoped CeO<sub>2</sub> specimen as the standard, and its Ce 3d spectra were deconvoluted using 11 components (see Fig. 4(b) for details). By performing similar treatments to Ca-doped CeO<sub>2</sub>, deconvolution results can be obtained, and an example from 50Ca is shown in Fig. 4(b). The relevant information (the peak shift, the full width at half maximum (FWHM) and the area fraction) for each component is listed in Table 1. From this information, the peak shift can be determined by comparing the BE values of all the components with the u" peak. Subsequently, by assuming that the undoped CeO<sub>2</sub> corresponds to a state with 100% Ce<sup>4+</sup>, the Ce<sup>4+</sup> fractions for the Cadoped samples were accordingly determined by adding the area fractions of all the eligible components, the peak shift of which equals the corresponding value of the undoped CeO<sub>2</sub> (error bar =  $\pm 0.4$  eV). As shown in Table 1, a general tendency can be noted that the higher the dopant concentrations, the smaller the fractions of the Ce<sup>4+</sup> state. This tendency suggests that severe reductions took place in heavily Ca-doped samples, e.g. about 30% for 50Ca

Fig. 5(a) presents the O 1s spectra for all samples and Fig. 5(b) shows the results of the analysis for the undoped CeO<sub>2</sub> and 50Ca (as an example to show the case for the Cadoped CeO<sub>2</sub>). As shown in Fig. 5(b), the O 1s spectrum of the undoped CeO<sub>2</sub> can be deconvoluted by two components: a higher BE (HBE) component at ~532 eV and a lower BE (LBE) component at ~529.5 eV. According to the XPS database [21], the HBE component can be ascribed to the absorbed oxygen, and therefore the LBE component should be contributed from the lattice  $O^{2-}$  in  $CeO_2$  ( $O^{2-}|_{CeO_2}$ ). In contrast, the O 1s spectrum for 50Ca is more broadly distributed, suggesting a more complicated chemical state. By using three components to fit the experimental spectrum, two components match with the aforementioned absorbed oxygen and O2-|CeO2, leaving an extra component at ~530.5 eV, which should be assigned to  $O^{2-}|_{secondary\ phase}$ . Subsequently, a parameter – the relative area fraction - was obtained by comparing the area

Table 1 Ce 3d spectra deconvolution results for the undoped  $CeO_2$  and 50Ca. Information on the peak shift, FWHM and area fraction of each component is provided.  $Ce^{4+}$  fractions for all Ca-doped  $CeO_2$  are also listed.

Peak shif	t (eV, erroi	within ±0.2	(V)								
$CeO_2$	0	-10.0	-13.0	-15.5	-17.5	-18.2	-27.6	-30.8	-33.7	-35.4	-36.3
50Ca	0	-10.0	-13.0	-15.7	-17.8	-18.3	-28.1	-30.9	-33.9	-34.7	-36.3
FWHM (	eV, error w	vithin ±0.2 eV	)								
$CeO_2$	2.7	4.8	2.8	2.8	2.8	2.9	4.5	3.1	3.1	3.1	3.1
50Ca	2.6	4.8	2.8	2.8	2.7	2.7	4.3	3.1	3.1	3.1	3.1
Area (%,	error withi	n ±0.5%)									
$CeO_2$	6.99	10.37	7.45	11.25	0.20	15.39	10.69	12.90	14.68	6.92	3.15
50Ca	7.26	11.01	8.61	12.8	0.78	13.49	12.31	11.30	15.05	4.68	2.70
Composition				5Ca		10Ca	20Ca	30Ca		40Ca	50Ca
$Ce^{4+}$ fraction (error within $\pm 5\%$ )				94.4%		88.0%	76.6%	73.9%	·	67.6%	70.2%

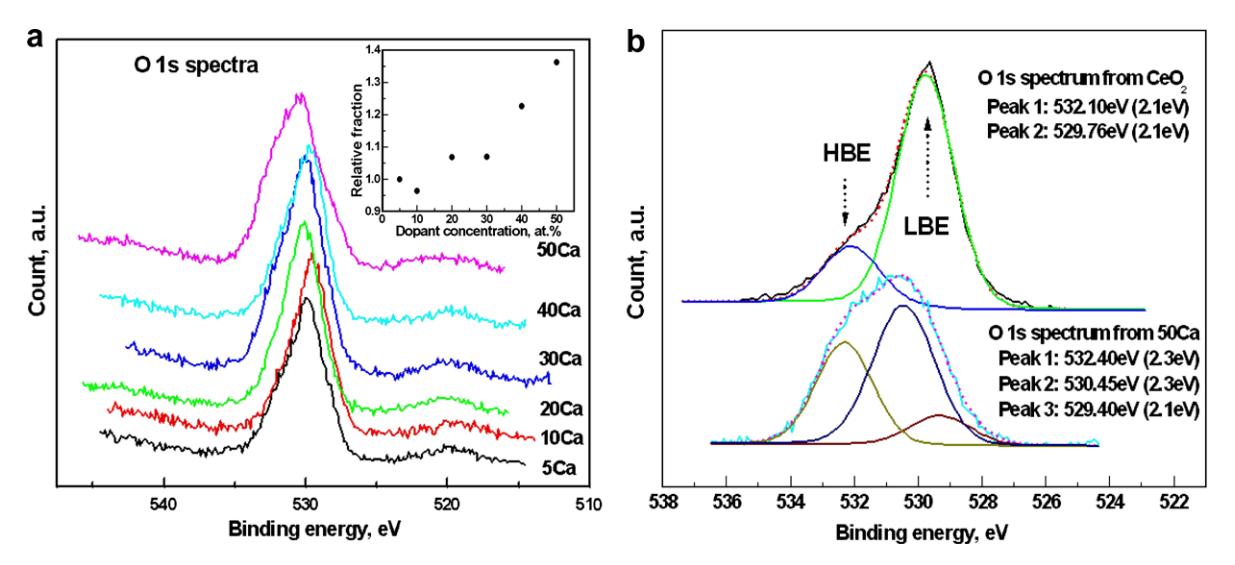


Fig. 5. XPS results for the sintered pellets: (a) O 1s spectra with an inset showing the relative area fraction (compared with 5Ca) of the  $O^{2-}|_{secondary\ phase}$  as a function of dopant concentration (error bar =  $\pm 5\%$ ) and (b) deconvolution results for the undoped CeO<sub>2</sub> and 50Ca. Peak positions and FWHM values (in the parentheses) are provided for each component. Dotted lines represent the fitting curves.

fraction of  $O^{2-}|_{secondary\ phase}$  in all dopant concentrations with that of 5Ca, and the relevant results are shown in the inset of Fig. 5(a), which shows a general tendency for the fraction of  $O^{2-}|_{secondary\ phase}$  to increase with increasing dopant concentration.

The Ca 2p spectra for all samples are shown in Fig. 6(a), with the deconvolution results for 50Ca being shown (as an example) in Fig. 6(b). This suggests that two pairs of components (an HBE pair and a LBE pair) can be deconvoluted for the Ca 2p spectrum. The HBE pair with 350.80 eV for Ca 2p 1/2 and 347.30 eV for Ca 2p 3/2 should be particularly closely related to the Ca-enriched secondary phase, since the Ca 2p 3/2 value for the standard  $Ca^{2+}|_{CaO}$  positions is at ~347.3 eV [21]. As a consequence,

the LBE pair must be ascribed to  $Ca^{2+}|_{CeO2}$ , having its 2p 1/2 and 2p 3/2 peaks positioned at ~350.1 and ~346.5 eV, respectively. By calculating the area fraction of the HBE components in the total Ca signals, it is noted that the HBE components increase their area fraction with increasing the dopant concentration (refer to the inset of Fig. 6(a)).

# 3.3. TEM analysis

So far, the aforementioned experimental results suggest two important issues for the Ca-doped CeO<sub>2</sub> materials: (i) the existence of a secondary phase(s) when the dopant concentration is sufficient and (ii) the reduction of

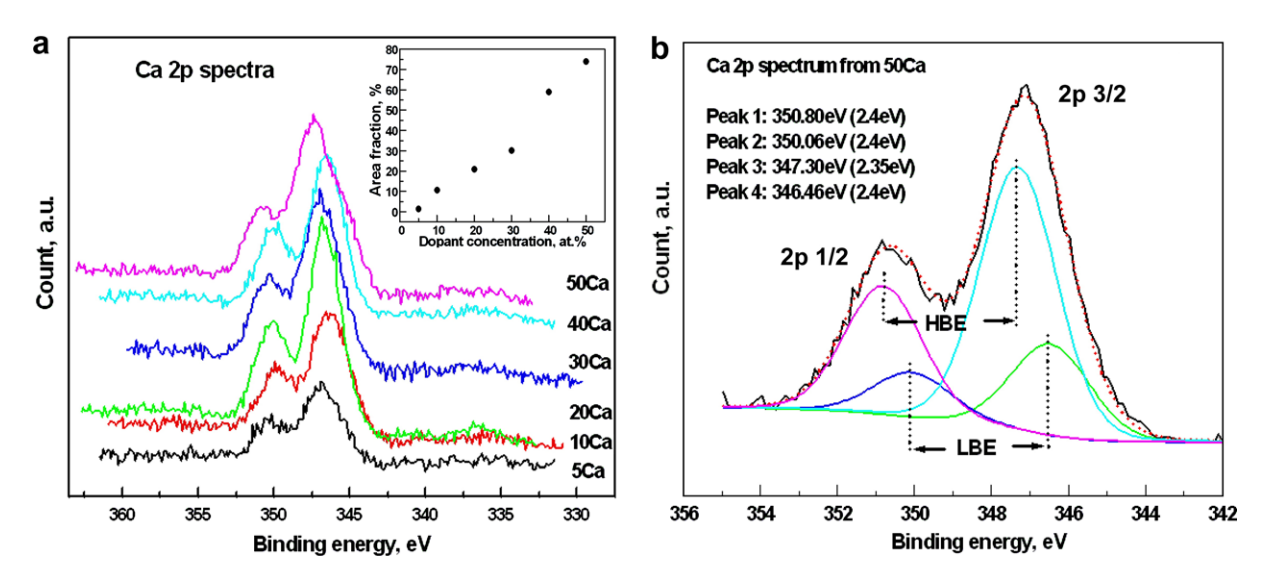


Fig. 6. XPS results for the sintered pellets: (a) Ca 2p spectra with an inset showing the area fraction of the HBE components in the total Ca signals as a function of the dopant concentration (error bar =  $\pm 5\%$ ) and (b) deconvolution results for 50Ca. Peak positions and FWHM values (in the parentheses) are provided for each component. Dotted lines represent the fitting curve.

Ca-doped  $CeO_2$  from  $Ce^{4+}$  alone to a mixed state of  $(Ce^{4+} + Ce^{3+})$ . To further clarify these two issues, a TEM study was performed.

Fig. 7(a) shows a bright-field TEM image and a series of selected area electron diffraction (SAED) patterns taken from a typical example of 30Ca. These SAED patterns can be ascribed to a face-centered cubic (fcc) structure. To determine the lattice parameter of this phase accurately, a thin layer of polycrystalline Au particles was coated on the surface of the TEM specimen, and their diffraction rings were used to calibrate the camera length due to the known lattice parameter of Au (a = 0.408 nm). From this, the lattice parameter of this phase was determined to be a = 0.54 nm, which is identical to the doped ceria.

Similar TEM investigations were also employed to determine the secondary phase. Fig. 7(b) shows a typical example of the secondary phase, with SAED patterns viewed along the same zone axes as shown in Fig. 7(a). Careful analysis of these diffraction patterns suggests that the secondary phase also belongs to an fcc structure with a lattice parameter of a = 0.48 nm, which is coincident with the CaO phase (a = 0.48 nm with PDF #00-037-1497).

As well as the doped ceria and the specified secondary phase, unusual SAED patterns were also observable in the samples with the dopant concentration higher than 5 at.%. Fig. 8(a) is a dark-field TEM image presenting such an example, while Fig. 8(b) gives the corresponding SAED pattern. As shown in Fig. 8(b), diffraction rings from the atomic planes of {111}\*Au, {111}\*CeO2 and {220}\*CeO2 can be indexed. There is also an additional diffraction ring that is located more closely to (000)\*, on which the dark-

field image in Fig. 8(a) was based. The lattice spacing of this diffraction ring was determined to be  $\sim 0.47$  nm, which matches perfectly with the  $\{211\}^*$  atomic planes of the body-centered cubic (bcc) structured  $Ce_2O_3$  (a=1.141 nm with PDF #01-072-6357). As suggested by the aforementioned XPS study, we believe the existence of this bcc  $Ce_2O_3$  phase resulted from the reduction of Ca-doped  $CeO_2$ . This finding is important for understanding the reduction behavior of the Ca-doped  $CeO_2$  materials, since even though  $CeO_2$  itself is well known for its redox phenomenon, it is difficult to determine the reduction products since there are over 20 forms of cerium oxides produced by different oxygen stoichiometries.

When tilting heavily Ca-doped samples inside TEM, additional SAED features can be observed. Fig. 9 shows the TEM result from 20Ca. Fig. 9(a) provides a brightfield TEM image for a typical grain. When SAED patterns collected along different zone axes (Figs. 9(b)-(h)), diffuse scatterings and additional diffraction spots can be seen in certain zone axes, with some marked in Fig. 9(c) and (e)-(g). Fig. 10 gives the corresponding index of these additional diffraction spots. In fact, it is generally believed that diffuse scatterings and additional reflections result from the crystal defects in materials like doped ceria and doped zirconia, reflecting the existences of microdomains and/or superstructures [13–16,25,26]. Consequently, it is anticipated that the high level of Ca doping leads to the formation of such crystal defects, and we believe that the current investigation is the first systematical study of these SAED features for Ca-doped CeO<sub>2</sub>.

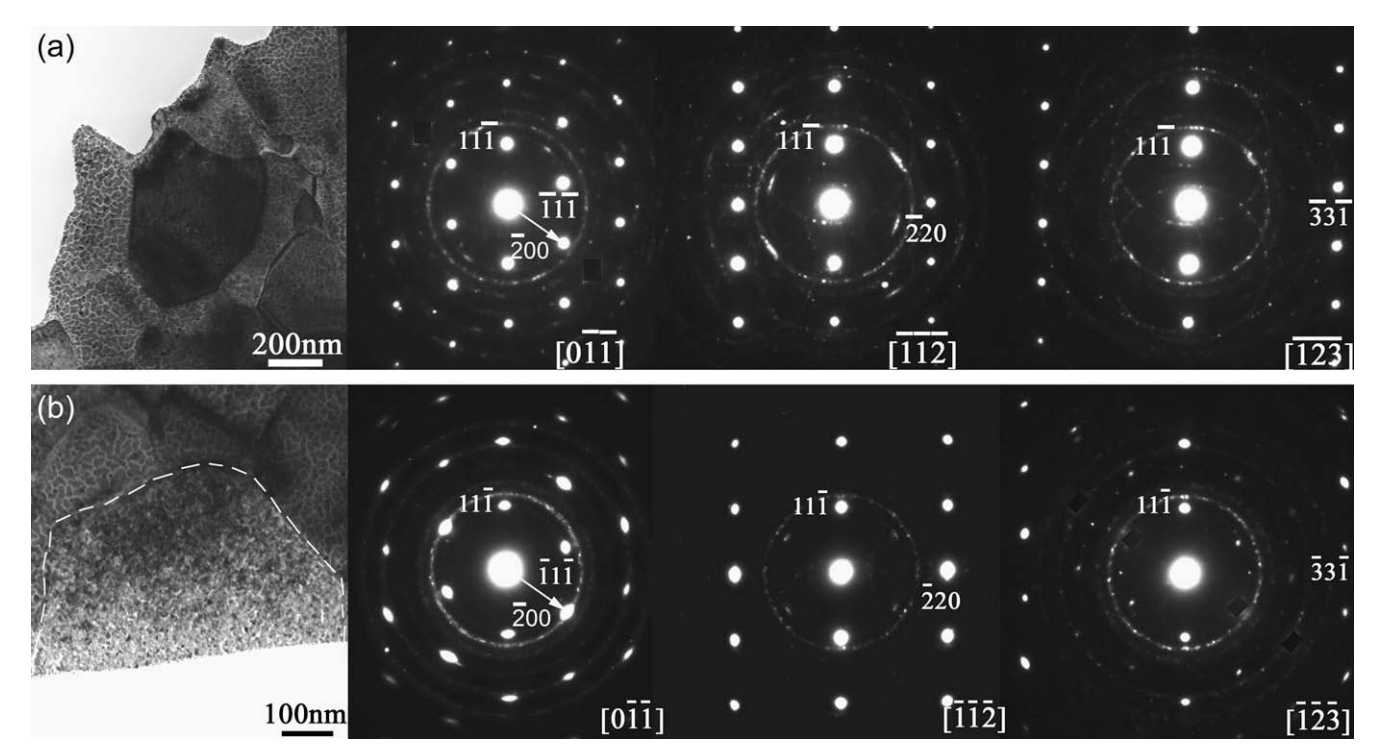


Fig. 7. TEM bright-field image and SAED patterns for (a) the doped ceria phase and (b) the secondary phase.

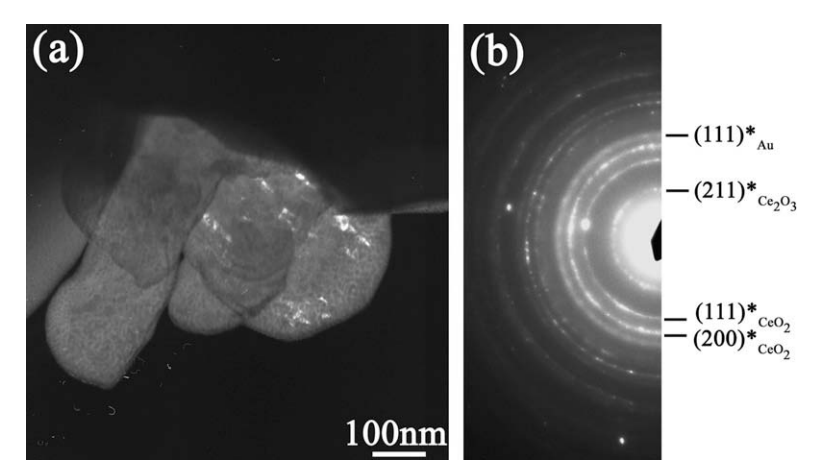


Fig. 8. TEM analysis of the reduced CeO<sub>2</sub> from 10Ca: (a) a dark-field image and (b) a corresponding SAED pattern and the corresponding index.

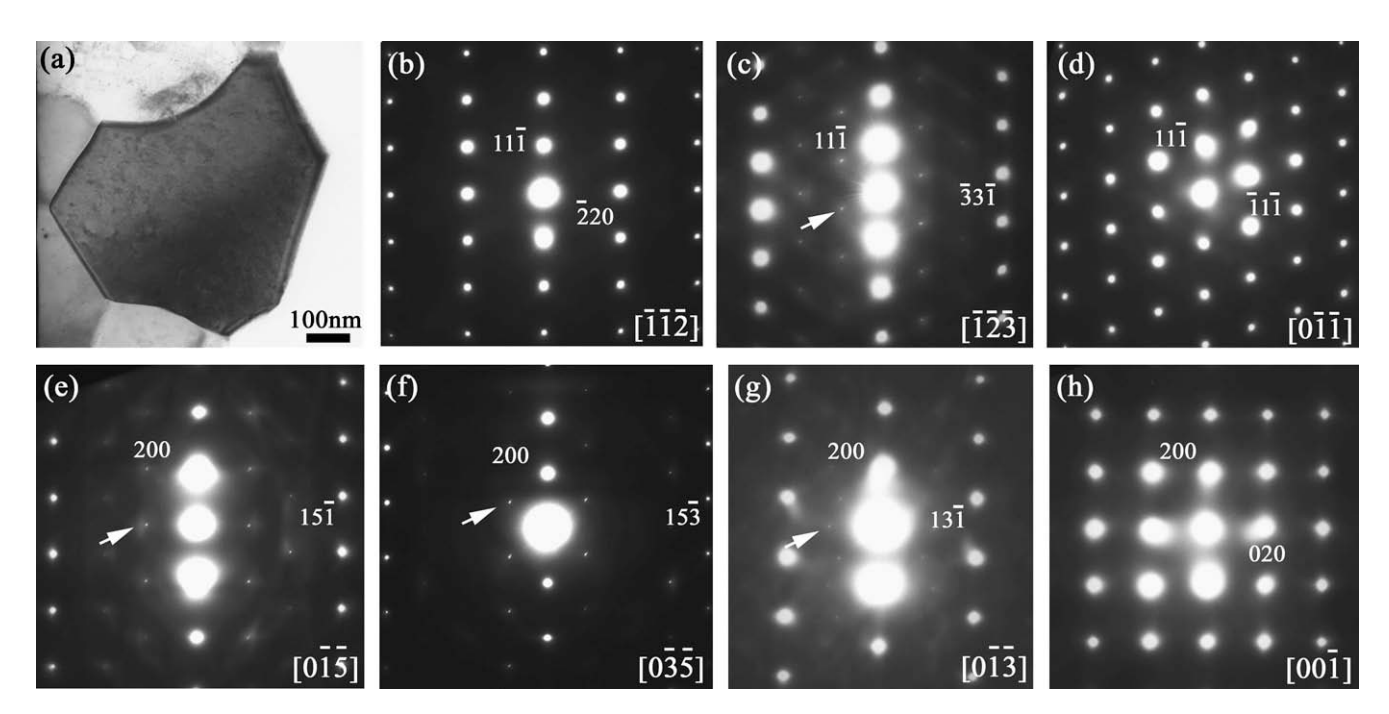


Fig. 9. TEM analysis of a typical phase in 20Ca: (a) a bright-field image and (b)–(h) SAED patterns in different zone axes. Additional reflections are marked by arrows.

During the TEM investigation, another interesting feature was observed in the heavily Ca-doped  $CeO_2$  and a typical example (taken from 40Ca) is presented in Fig. 11, showing a bright-field TEM image (Fig. 11(a)), a dark-field TEM image (Fig. 11(b)), an SAED pattern along the zone axis of [110] (Fig. 11(c)) and the corresponding index (Fig. 11(d)). As shown by Fig. 11(c), abnormal diffraction spots (corresponding to almost three times the lattice spacing of  $d_{(111)}*|_{CeO2}$ ) were observed. Interestingly, these abnormal diffraction spots disappeared when the TEM specimen was tilted on the other zone axes (see e.g. the inset of Fig. 11(a), where the zone axis is [123]). Based on this, we believe that the possibility of other crystalline phases responsible for such an SAED feature is small, since otherwise regular SAED patterns would also be observable in other zone axes. Careful

analysis of these abnormal diffraction spots, shown in Fig. 11(d), indicates that they are not perfectly aligned with the main diffraction spots. As a consequence, they might be satellite spots caused by a double diffraction between the grain and ordered crystalline defects, such as vacancy defects. The existence of such a microstructure therefore suggests that high dopant concentrations can also introduce extra ordered defects into the Ca-doped CeO<sub>2</sub> materials.

## 4. Discussion

In the Ca-doped  $CeO_2$  system, if the charge balance and the occupancy of  $Ca^{2+}$  in the position of  $Ce^{4+}$  are considered, the dissolved CaO might interact with  $CeO_2$  in the following manner:

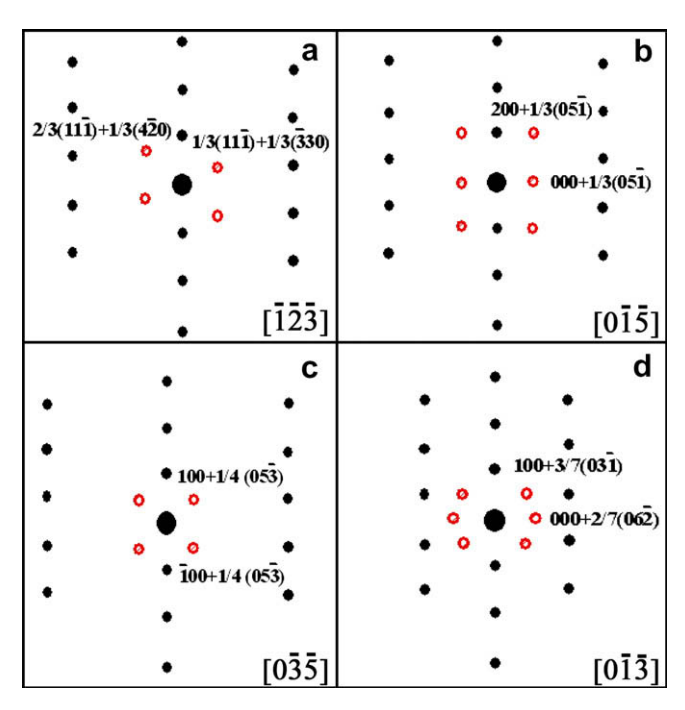


Fig. 10. Schematic graphs showing the index of the additional reflections in the zone axes of: (a)  $[\bar{1}\,\bar{2}\,\bar{3}]$ , (b)  $[0\,\bar{1}\,\bar{5}]$ , (c)  $[0\,\bar{3}\,\bar{5}]$  and (d)  $[0\,\bar{1}\,\bar{3}]$ .

$$2\text{CaO} + 2\text{CeO}_2 = 3\text{O}_2 + 3V_0'' + 2\text{Ce}_{\text{Ce}}' + 2\text{Ca}_{\text{Ce}}''$$
 (1)

where  $V_o^{\circ}$  stands for the positively charged bivalent oxygen vacancy,  $Ce'_{Ce}$  for the negatively charged monovalent reduced Ce, and  $Ca''_{Ce}$  for the negatively charged bivalent Ca in the lattice of  $CeO_2$ . Accordingly, three consequences are possible: (i) the formation of the oxygen vacancy  $(V_o^{\circ})$ ; (ii) the reduction of the  $CeO_2$  ( $Ce'_{Ce}$ ) and (iii) the formation of crystalline defects ( $Ca''_{Ce}$ ). In the case of high dopant concentrations (beyond the solubility limit of Ca in  $CeO_2$ ), a secondary phase(s) is also expected. Among these factors, the formation of oxygen vacancy is a common phenomenon for doped ceria materials [5], so is not the focus of this study. Since the detailed TEM and XPS characterizations of the secondary phase, the crystalline defects and the reduction behavior of Ca-doped  $CeO_2$  have not been reported previously, they need to be clarified.

As outlined above, the secondary phase was determined to be the fcc-structured CaO by TEM, consistent with previous studies (e.g. [7]). Controversy still exists, however, with respect to the solubility limit of the dopant. In other previous studies [27,28], 20–23 at.% of Ca in CeO<sub>2</sub> was believed to be the solubility limit. However, the secondary phase has been repeatedly observed in 20Ca (an example is

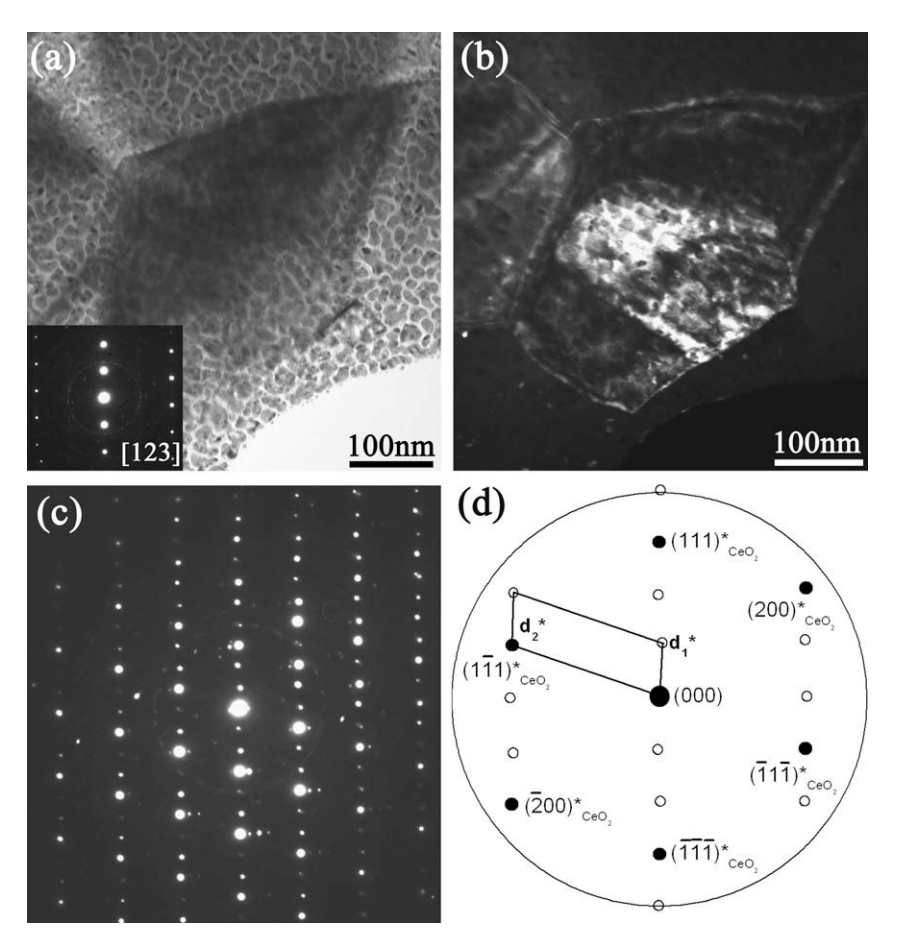


Fig. 11. TEM analysis of the crystal defect from 40Ca: (a) a bright-field image, (b) a dark-field image, (c) an SAED pattern in the zone axis of [110] of the doped CeO<sub>2</sub> and (d) an indexing graph of the SAED pattern. The inset in (a) shows an SAED pattern in the zone axis of [123].

Table 2 Conductivity property of Ca-doped CeO<sub>2</sub> with different dopnat concentrations (400-700 °C as the measurement region,  $\sigma$  at 500 °C).

Composition	5Ca	10Ca	20Ca	30Ca	40Ca	50Ca
$\log \sigma$ , S cm <sup>-1</sup> (error within $\pm 0.01$ )	-3.367	-3.317	-3.486	-3.564	-3.563	-3.602

shown by the SEM-BSE image in Fig. 2(b)), suggesting that the solubility limit of Ca in CeO<sub>2</sub> should be less than 20 at.% under our sintering pathway. One possible reason for the discrepancy in the solubility could be that, in the studies, higher sintering previous temperatures  $(\sim 1400 \, ^{\circ}\text{C})$  were usually used. Even though the solubility is dependent on the sintering temperature, however, a study of the ternary MgO-CaO-CeO2 system suggested an even high temperature of 1700 °C was required to secure a 20 at.% Ca solubility in CeO<sub>2</sub> [29]. Our unpublished results on the sintering behavior of Ca-doped CeO<sub>2</sub> (sintering temperature up to 1400 °C) confirm this point.

It is believed that CaO is an isolating phase in terms of the ionic conductivity for the Ca-doped CeO<sub>2</sub> [5]. The crystalline defects in the form of microdomains and/or superstructures that are expected in the heavily Ca-doped samples should also have a negative impact on the ionic conductivity [13–16,26]. Consequently, a high dopant concentration will create isolating secondary phases and crystalline defects, and cause severe reductions in CeO<sub>2</sub>; all these considerably undermining the ionic conductivity of Ca-doped CeO<sub>2</sub>. Meanwhile, since the doped Ca decides the amount of the charge carrier for ionic conductivity as described by the following equation, a sufficient concentration of Ca is needed to maximize the conductivity [5].

$$\sigma_i = \sum n_i q_i \mu_i \tag{2}$$

where  $\sigma_i$  is the ionic conductivity, and  $q_i$ ,  $n_i$  and  $\mu_i$  are the charge, concentration and mobility of the charge carriers, respectively. As a consequence, 5 at.% Ca may not provide enough charge carriers, and a doping level around 10 at.% might be appropriate for the Ca-doped CeO<sub>2</sub> materials to achieve the optimum ionic conductivity. Table 2, which lists the measured conductivity properties ( $\sigma$ ) of different Ca-doped CeO<sub>2</sub> samples (at 500 °C), confirms this point. It can be seen from the table that the maximum conductivity is found in 10Ca.

In terms of the reduction behavior of Ca-doped CeO<sub>2</sub>, an interesting XPS result (see Table 1) is that the Ce<sup>4+</sup> fraction remains comparatively stable at dopant concentrations ranging from 20 to 50 at.%. This is due to the solubility of Ca in CeO<sub>2</sub>, which requires no further substitution of Ce by Ca when the solution limit is surpassed. Based on the deconvolution results for the O 1s spectrum shown in Fig. 5(b), another noticeable feature of the XPS results is that the BE of O 1s is at  $\sim$ 530.5 eV for O<sup>2-</sup>|secondary phase, which is lower than the standard value of the lattice O<sup>2-</sup> in CaO (531.7 eV [21]). A possible reason for this is that the composition of the secondary phase has deviated from the nominal CaO, even though the secondary phase adopts the same crystal structure as CaO, as

confirmed by our SAED study. As a consequence, this leads to a discrepancy in its electronic state when compared with the standard  $O^{2-}|_{CaO}$ , making its BE move towards the value of  $O^{2-}|_{CeO^2}$ .

## 5. Conclusions

From a systematic investigation of the microstructure and ionic conductivity of Ca-doped CeO<sub>2</sub>, we can draw the following conclusions:

- (1) When the dopant concentration is beyond the solubility limit of Ca in CeO<sub>2</sub>, an fcc-structured secondary phase (CaO) results, as confirmed by the TEM-SAED study. In the heavily Ca-doped CeO<sub>2</sub>, crystalline defects in the form of microdomains and/or super-structures are observed. Under the current low-temperature sintering pathway, it has been found that 10 at.% Ca doping provides optimal ionic conductivity.
- (2) A quantitative determination of CeO<sub>2</sub> reduction induced by Ca doping in a wide dopant concentration range (from 5 to 50 at.%) has been achieved through systematic XPS investigations. The results suggest that severe reductions can occur in heavily Ca-doped CeO<sub>2</sub>. The XPS study also provides the chemical state information for the O and Ca elements, in both the secondary phase (CaO) and the matrix doped CeO<sub>2</sub> phase.
- (3) The product of the reduction of Ca-doped  $CeO_2$  was determined to be bcc-structured  $Ce_2O_3$  (a = 1.141 nm, PDF #01-072-6357).

## Acknowledgement

We acknowledge the kind assistance of Dr. Mingren Sun from Harbin Institute of Technology (China) with the XPS measurements.

#### References

- [1] Mogensen M, Sammes NM, Tompsett GA. Solid State Ionics 2000;129:63.
- [2] Steele BCH. In: Takahashi T, editor. High conductivity solid ionic conductors recent trends and applications. London: World Scientific; 1989. p. 402.
- [3] Guio M, Prieto J, Corberan VC. Catalysis Today 2006;112:148.
- [4] Izu N, Shin W, Matsubara I, Murayama N. Sensor Actuat B-Chem 2004;101:381.
- [5] Inaba H, Tagawa H. Solid State Ionics 1996;83:1.
- [6] Balazs GB, Glass RS. Solid Sate Ionics 1995;76:155.
- [7] Arai H, Kunisaki T, Shimizu Y, Seiyama T. Solid State Ionics 1986;20:241.

- [8] Zhu B, Liu XR, Sun MT, Ji SJ, Sun JC. Solid State Sci 2003;5:1127.
- [9] Lu Z, Huang XQ, Liu W, He TM, Liu ZG, Liu J, et al. J Rare Earths 2002:20:47.
- [10] Garnier JE, Blumenthal RN, Panlener RJ, Sharma RK. J Phys Chem Solids 1976;37:369.
- [11] Wang DY, Nowick AS. J Solid State Chem 1980;35:325.
- [12] Hurley MD, Hohnke DK. J Phys Chem Solids 1980;41:1349.
- [13] Ye F, Mori T, Ou DR, Takahashi M, Zou J, Drennan J. J Electrochem Soc 2007;154:B180.
- [14] Ou DR, Mori T, Ye F, Zou J, Auchterlonie G, Drennan J. Electrochem Solid-State Lett 2007:10:1.
- [15] Mori T, Wang YR, Drennan J, Auchterlonie G, Li JG, Ikegami T. Solid State Ionics 2004;175:641.
- [16] Mori T, Drennan J, Wang YR, Auchterlonie G, Li JG, Yago A. Sci Tech Adv Mater 2003;4:213.
- [17] Zhang F, Wang P, Koberstein J, Khalid S, Chan SW. Surf Sci 2004;563:74.

- [18] Borchert H, Borchert Y, Kaichev VV, Prosvirin IP, Alikina GM, Lukashevich AI, et al. J Phys Chem B 2005;109:20077.
- [19] Yan M, Mori T, Ye F, Ou DR, Zou J, Drennan J. J Euro Ceram Soc 2008;28:2709.
- [20] Wang YR, Mori T, Li JG, Ikegami T, Yajima Y. J Mater Res 2003;18:1239.
- [21] Crist BV. In: Handbook of monochromatic XPS spectra in the elements and native oxides. John Wiley & Sons; 2000.
- [22] Paparazzo E. J Vac Sci Technol A 2004;22:2188.
- [23] Hoang M, Hughes AE, Turney TW. Appl Surf Sci 1993;72:55.
- [24] Holgado JP, Alvarez R, Munuera G. Appl Surf Sci 2000;161:301.
- [25] Garcia-Martin S, Alario-Franco MA, Fagg DP, Feighery AJ, Irvine JTS. Chem Mater 2000;12:1729.
- [26] Drennan J, Auchterlonie G. Solid State Ionics 2000;134:75.
- [27] Eguchi K, Kunisaki T, Arai H. J Am Ceram Soc 1986;69:C282.
- [28] Yahiro H, Ohuchi T, Eguchi K, Arai H. J Mater Sci 1988;23:1036.
- [29] Longo V, Podda L. J Am Ceram Soc 1978;61:370.